Optics and Lasers in Engineering 139 (2021) 106475

Contents lists available at ScienceDirect

Optics and Lasers in Engineering

journal homepage: www.elsevier.com/locate/optlaseng

Total variation and block-matching 3D filtering-based image reconstruction for single-shot compressed ultrafast photography

Jiali Yao [1], Dalong Qi [1,*], Yunhua Yao [1], Fengyan Cao [1], Yilin He [1], Pengpeng Ding [1], Chengzhi Jin [1], Tianqing Jia [1,*], Jinyang Liang [2], Lianzhong Deng [1], Zhenrong Sun [1], Shian Zhang [1,3,4,*]

[1] State Key Laboratory of Precision Spectroscopy, School of Physics and Electronic Science, East China Normal University, Shanghai, 200062, China
[2] Laboratory of Applied Computational Imaging, Centre Énergie Matériaux Télécommunications, Institut National de la Recherche Scientifique, Varennes, Québec, J3 × 1S2, Canada
[3] Collaborative Innovation Center of Extreme Optics, Shanxi University, Taiyuan, 030006, China
[4] Collaborative Innovation Center of Light Manipulations and Applications, Shandong Normal University, Jinan, 250358, China

ARTICLE INFO

Keywords:
Optical imaging
Computational imaging
Compressed sensing
Image denoising

ABSTRACT

Compressed ultrafast photography (CUP), as the fastest receive-only ultrafast imaging technology by combining steak imaging and compressed sensing (CS), has shown to be a powerful tool to measure ultrafast dynamic scenes. Through a reconstruction algorithm based on CS, CUP can capture the three-dimensional image information of non-repetitive transient events with a single exposure. However, it still suffers from poor image reconstruction quality on account of the super-high data compression ratio induced by the undersampling strategy. Here, we propose a total variation (TV) combined with block matching and 3D filtering (BM3D) reconstruction algorithm to improve the image quality of CUP, which is named as the TV-BM3D algorithm. The proposed algorithm can simultaneously exploit gradient sparsity and non-local similarity for image reconstruction by incorporating TV and BM3D denoisers. Both the numerical simulations and experimental results show that, compared with the two conventional two-step iterative shrinkage/thresholding and augmented Lagrangian algorithms in CUP, the TV-BM3D algorithm can not only improve the image reconstruction quality, but also strengthen the noise immunity of this technique. It is prospected that these improvements in image reconstruction will further promote the practical applications of CUP in capturing complex physical and biological dynamics.

1. Introduction

Single-shot ultrafast optical imaging is an important branch in the ultrafast optical imaging field. This technology can capture non-repeatable or difficult-to-repeat ultrafast dynamic events in real time, which offers an imaging speed over three orders of magnitude higher than that of charge-coupled device (CCD) or complementary metal-oxide-semiconductor (CMOS) detectors. Therefore, it has significant applications in not only scientific but also industrial and military fields [1]. Single-shot ultrafast optical imaging based on passive detection, which requires no specific active illumination, is widely used to record photoluminescent, chemiluminescent and color-selective transient scenes. According to ways of obtaining the images of recorded objects, there are two general techniques: direct imaging and reconstruction imaging. The direct imaging techniques, such as ultrafast framing cameras [2] and high-speed sampling cameras [3], have succeeded in capturing shockwave dynamics [4], electron energy transport [5] and plasma dynamics [6]. However, they still suffer from either a poor sequence depth, i.e., the number of images per shot, or very few pixel counts per image. To overcome these limitations, compressive sensing-based reconstruction approaches including compressed ultrafast photography (CUP) [7-9] and multi-aperture compressed sensing CMOS [10] have been proposed to vastly compress the data throughput by taking advantage of the sparsity of dynamic scenes.

By combining compressed sensing algorithms with the streak camera, CUP develops as a single-shot and receive-only imaging approach requiring no active illumination and capable of capturing ultrafast time-evolution events at speeds up to 10^{13} frames per second with a sequence depth of several hundred frames. Since its proposal, CUP has attracted great attention from scientists. To date, this technology has been successfully applied in capturing flying photons [7,11], measuring the spatiotemporal intensity of ultrashort laser fields [8,12], recording four-dimensional information simultaneously [13], and phase-sensitive imaging [14].

* Corresponding authors.
E-mail addresses: dlqi@lps.ecnu.edu.cn (D. Qi), tqjia@phy.ecnu.edu.cn (T. Jia), sazhang@phy.ecnu.edu.cn (S. Zhang).

https://doi.org/10.1016/j.optlaseng.2020.106475
Received 2 September 2020; Received in revised form 9 October 2020; Accepted 10 November 2020
Available online 22 November 2020
0143-8166/

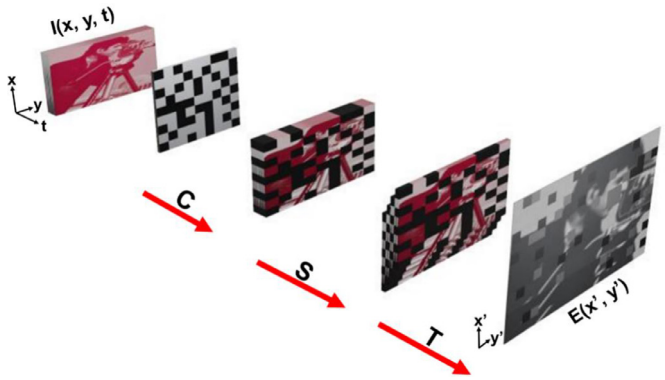

Fig. 1. Schematic diagram of data acquisition for CUP, where, *t*: time; *x, y*: spatial coordinates of the dynamical scene; *x′, y′*: spatial coordinates at the streak camera; C: spatial encoding operator; S: temporal shearing operator; and T: spatiotemporal integration operator.

In CUP's operation, the three-dimensional (3D) *x-y-t* information of a dynamic scene is first captured by a streak camera after random encoding, and then the CS algorithm is used to recover the original dynamic scene. During the image acquisition, the target scene has a rather high portion of its information lost due to pseudo-random binary encoding, which makes the CUP a kind of lossy imaging. In addition, the target information is inevitably polluted by noise during the image acquisition. Therefore, the finally reconstructed images are often of poor quality and low accuracy. In order to make up for these defects, various improving methods have been proposed in recent years, such as the spatial and strength constraint reconstruction algorithm [15], the optimization of the encoding pattern method [16], and the augmented Lagrangian (AL) algorithm [17]. However, all these algorithms exploit total variation (TV) as the regularization function, which means that gradient sparsity is utilized as the main prior information for image reconstruction. Here, we report a symphysic algorithm jointly based on TV and block matching and 3D filtering (BM3D), named as the TV-BM3D algorithm. In this algorithm, the generalized alternating projection (GAP) framework is adopted [18], and TV and BM3D denoisers are employed to solve the image denoising sub-problem. Compared with the algorithms based on TV regularization, The TV-BM3D algorithm simultaneously exploits the sparsity in the gradient domain and non-local similarity of images to ensure a higher reconstruction quality. In this paper, the TV-BM3D algorithm is also compared to the two conventional algorithms based on TV regularization, i.e. AL algorithm [17] and two-step iterative shrinkage/thresholding (TwIST) algorithm [19], in image reconstruction. We numerically simulate a moving Shepp–Logan (S–L) phantom in space and a rotating fan polluted by various noise levels, and experimentally measure a spatially modulated picosecond laser pulse. Both the simulation and experimental results demonstrate the effectiveness of our proposed algorithm.

2. Methods

In a CUP system, the target dynamic scene is first randomly encoded in space and then sheared sequentially by a streak camera according to its time of arrival at the detector. Finally, a CCD camera spatiotemporally integrates all the temporally sheared images under a single shot exposure. As shown in Fig. 1, a 3D *x-y-t* data cube representing the target dynamic scene is transformed into a two-dimensional (2D) *x′-y′* image to be captured by the CCD. Considering the noise introduced by the measurement device, the image acquisition process can be modeled as [7]:

$$E(x', y') = \mathrm{TSC}I(x, y, t) + n = \mathrm{O}I(x, y, t) + n, \tag{1}$$

where $I(x, y, t)$ is target dynamic scene with N elements, $E(x', y')$ is a noisy observation with M elements captured by CCD. C, S and T are spatial encoding, temporal shearing and spatiotemporal integration operators, respectively. The analytical expressions of operators C, S, T can be found in Ref. [9]. O is a combined linear operator, and n represents noise.

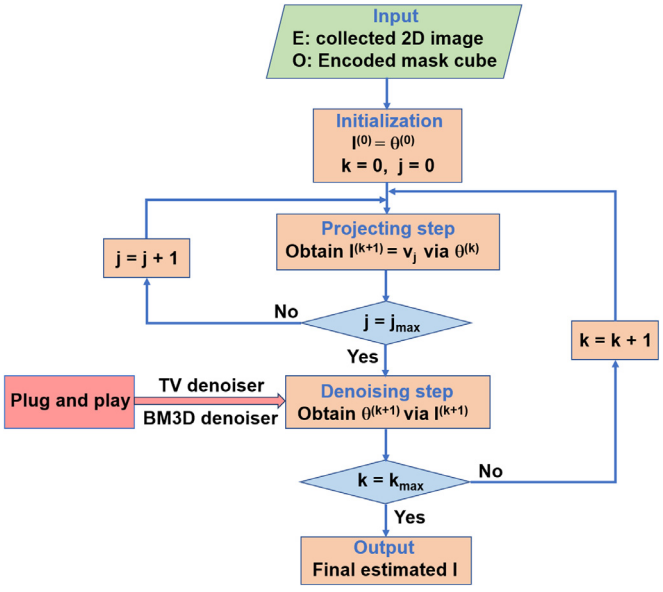

Fig. 2. Flow chart of the TV-BM3D algorithm.

In order to obtain the target dynamic scene, $I(x, y, t)$ needs to be recovered from $E(x', y')$, which requires solving Equation (1) in reverse. Typically, M is much smaller than N, thus the inverse problem is ill-posed, and priors about $I(x, y, t)$ are often needed. One way is to solve a constrained optimization problem [20], which can be expressed as:

$$\min_{I} \Phi(I) \text{s.t.} \|\mathrm{O}I - E\|_2^2 \le \varepsilon, \tag{2}$$

where $\Phi(I)$ is the regularizer representing the prior information, $||.||_2$ is the l_2 norm, and ε is a positive parameter dependent on noise level.

We extend the GAP method of Ref. [18] to the above optimization problem with an inequality constraint, and the problem (2) can be expressed equivalently as:

$$\min_{I,\delta} \text{s.t.} \Phi(I) \le \delta \text{and} \|\mathrm{O}I - E\|_2^2 \le \varepsilon, \tag{3}$$

where δ is the radius of the generalized $l_{1,2}$-ball based on $\Phi(I)$. Furthermore, by introducing an auxiliary variable θ, problem (3) can be rewritten as:

$$\min_{I,\theta,\delta} \|I - \theta\|_2^2 \text{s.t.} \Phi(\theta) \le \delta \text{and} \|\mathrm{O}I - E\|_2^2 \le \varepsilon, \tag{4}$$

which is equivalent to

$$\min_{I,\theta} \|I - \theta\|_2^2 + \lambda\Phi(\theta) \text{s.t.} \|\mathrm{O}I - E\|_2^2 \le \varepsilon, \tag{5}$$

where λ is the regularization parameter. In fact, this problem can be solved by alternately updating I and θ, which means that one parameter can be fixed while the other is being updated. Thus, the optimization can be represented by the following two separated iteration equations:

$$I^{(k+1)} = \arg\min_{I} \left\{ \left\| \theta^{(k)} - I \right\|_2^2 \right\} \text{s.t.} \|\mathrm{O}I - E\|_2^2 \le \varepsilon, \tag{6}$$

$$\theta^{(k+1)} = \arg\min_{\theta} \left\{ \left\| \theta - I^{(k+1)} \right\|_2^2 + \lambda\Phi(\theta) \right\}, \tag{7}$$

where k denotes the kth iteration. For convenience, we define $\mathrm{f}(\mathrm{I}) = ||\mathrm{OI} - \mathrm{E}||_2^2$.

On one hand, Equation (6) is a projection problem that can be solved by an epigraph set method [21]. Here, I and E are reshaped to vectors in

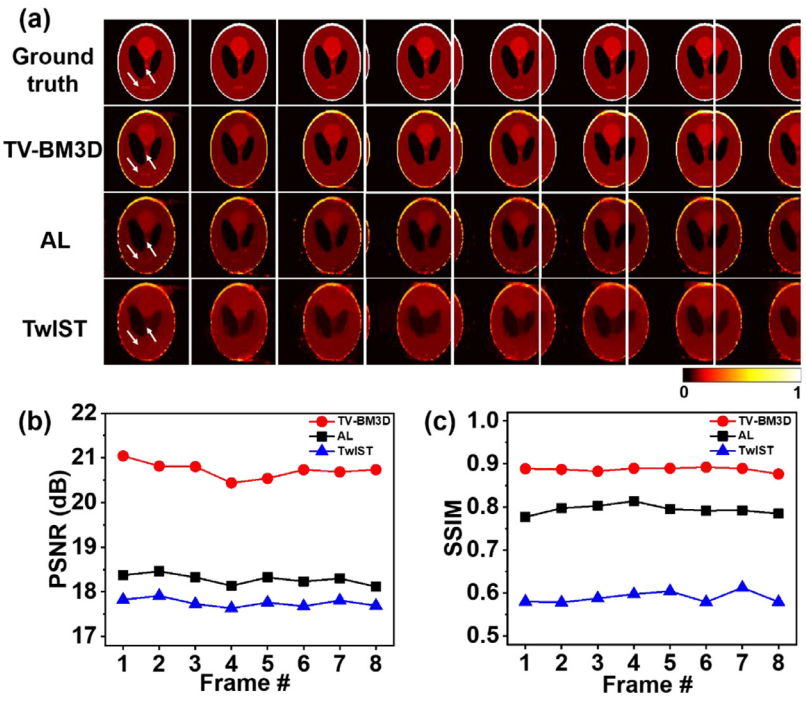

Fig. 3. Numerical simulation of a moving S-L phantom. (a) The original S-L phantom moving to right and the reconstructed S-L phantom from the TV-BM3D, AL and TwIST algorithms, respectively. (b) PSNR (dB) and (c) SSIM results of images reconstructed by the TV-BM3D (red circles), AL (black squares) and TwIST (blue triangles) algorithms, respectively.

operation. This method can handle Equation (6) by solving the following projection equation:

$$\underline{I}^{(k+1)} = \arg\min_{\underline{I}\in G} \left\{ \left\| \underline{\theta}^{(k)} - \underline{I} \right\|_2^2 \right\} \in \mathbb{R}^{N+1}, \tag{8}$$

where the underlined characters denote N+1 dimensional vectors, $\underline{\theta}^{(k)} = [\theta^{(k)T}\ 0]^T \in \mathrm{R}^{N+1}$, G is the epigraph set of $f(I)$ and defined as $G=\{[I^T\ q]^T \in \mathrm{R}^{N+1}: q \geq f(I)\}$ with q being a positive constant. It can be seen that the (N+1)th component q of vectors in the epigraph set G is no less than $f(I)$. To optimize Equation (8), we select the nearest vector $\underline{I}^{(k+1)}$ on the epigraph set G to $\underline{\theta}^{(k)}$, which requires performing successive orthogonal projections onto supporting hyperplanes of the set G. Here, a gradient descent method in Ref. [22] is used to calculate the projection point $[v_j{}^T\ f(v_j)]^T$ after the jth projection, and v_j can be expressed as:

$$v_j = v_{j-1} - \left[f(v_{j-1}) / \left(\left\| f(v_{j-1}) \right\|_2^2 + 1 \right) \right] \nabla f(v_{j-1}). \tag{9}$$

Here, the initial value of v_0 is set equal to $\theta^{(k)}$, $\nabla f(v_{j-1})$ denotes the derivative of the function f at the point v_{j-1} and can be expressed as $\nabla f(v_{j-1}) = 2O^T(Ov_{j-1} - E)$. After j_{max} times of successive projections in total, the final orthogonal projection onto the supporting hyperplane of the epigraph set, i.e., the optimized $\underline{I}^{(k+1)}$ of Equation (8), can be written as $[v_{jmax}{}^T\ f(v_{jmax})]^T$. Therefore, we can obtain $I^{(k+1)} = v_{jmax}$ after a reshaping from vector to matrix in Equation (7).

On the other hand, Equation (7) can be seen as a denoising problem with $I^{(k+1)}$ being a noisy image and $\theta^{(k+1)}$ the denoised image. Any effective image denoising algorithm can be used to solve Equation (7), thus this step is plug and play. Moreover, one can utilize multiple denoisers in parallel or alternately on solving Equation (7) to further improve the image reconstruction quality. Here, we use TV denoiser [23] and BM3D denoiser [24] alternately, i.e., TV denoiser in the first iteration and BM3D denoiser in the successive one. Theoretically, different denoisers demand different priors. When TV denoiser is selected, the gradient sparsity is exploited as the prior information, while the use of BM3D denoiser requires the non-local similarity and the sparsity under a 3D sparsifying transform being exploited as the prior information for image reconstruction. Therefore, the use of multiple denoisers means that richer priors are utilized. In each iteration, we adaptively update the noise standard deviation σ by following the rule proposed in Ref. [25]:

computing $\Delta^{(k+1)} = \frac{1}{\sqrt{N}}(\| I^{(k+1)} - I^{(k)} \|_2 + \| \theta^{(k+1)} - \theta^{(k)} \|_2)$,
and if $\Delta^{(k+1)} \geq \eta\Delta^{(k)}$, then $\sigma^{(k+1)} = \xi\sigma^{(k)}$,
if $\Delta^{(k+1)} < \eta\Delta^{(k)}$, then $\sigma^{(k+1)} = \sigma^{(k)}$,

where $\eta \in [0,1)$, with $\xi < 1$.

So far, both the I sub-problem and the θ sub-problem are solved. When $k = k_{max}$, the alternate update between I and θ is completed and the final output I is arranged as a 3D data cube for display. For clarification, a flow chart of the proposed TV-BM3D algorithm is shown in Fig. 2.

3. Results and discussions

To validate the reconstruction performance of the TV-BM3D algorithm, we create two different types of dynamic scenes for simulation in the CUP modality. Each frame of the dynamic scene is encoded by a standard pseudo-random binary mask with entries {0, 1}, and the pixel size of the mask is the same as that of the CCD camera. Then these encoded images from the dynamic scene are shifted sequentially with each frame moved down by one pixel relative to the previous one. Finally, all frames are integrated along the time axis to obtain the final 2D observation image.

The first dynamic scene is a S-L phantom moving to the right, which contains 8 images of size 150 × 150, as shown in the ground truth in Fig. 3(a). The intensity of the target object remains unchanged during the movement. The TV-BM3D, AL and TwIST algorithms have been respectively used to reconstruct the dynamic scene, and corresponding results are shown in Fig. 3(a). Obviously, the results reconstructed by the TV-BM3D algorithm are the best, while those from the AL and TwIST algorithms gradually become poor in image quality. This can also be better seen from the areas of the images pointed by the white arrows. Remarkable contrast of the compared areas can be seen for images reconstructed by the TV-BM3D algorithm. This contrast gets weak for images from the AL algorithm and disappears almost for results from the TwIST algorithm. In addition, both the TwIST and AL algorithms bring

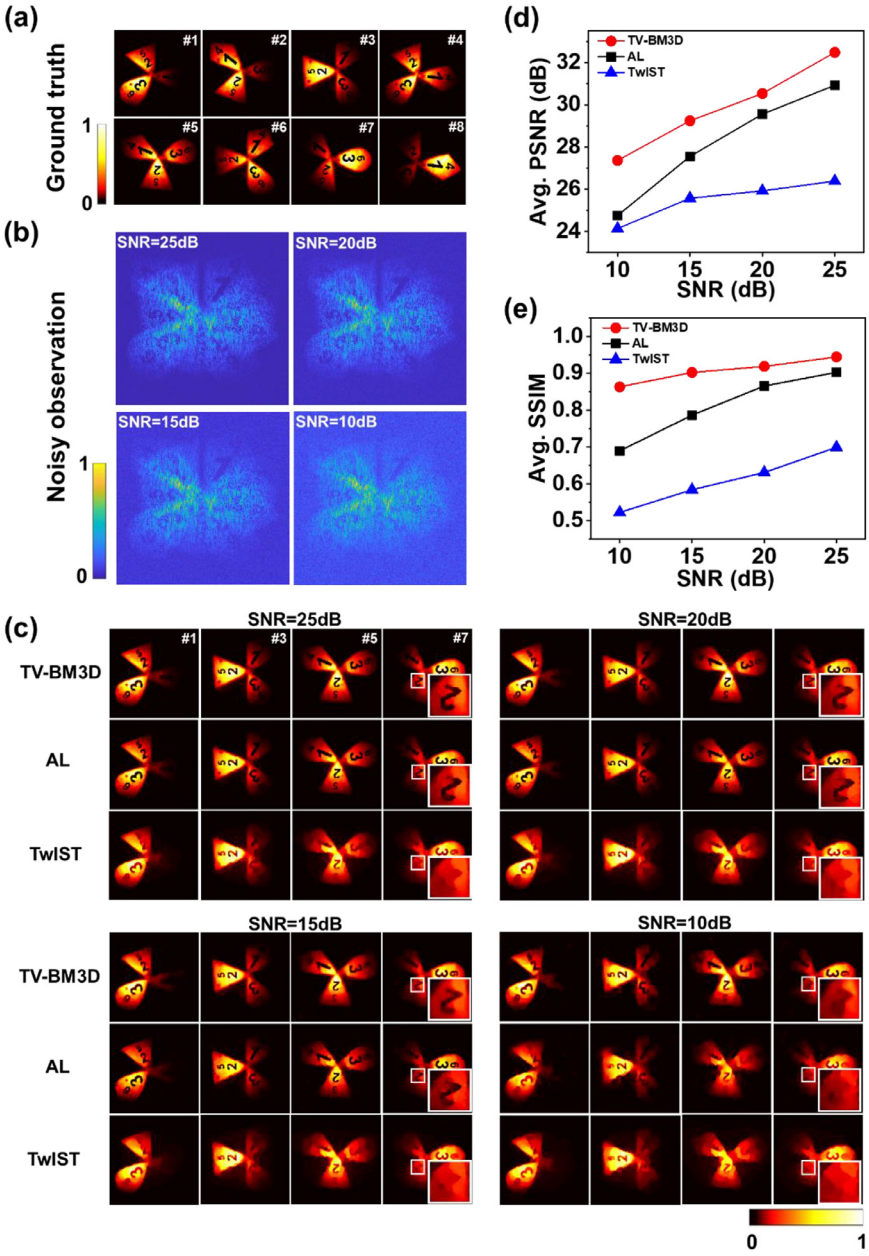

Fig. 4. Numerical simulation of a rotating fan. (a) The ground truth images of a rotating fan, (b) the sheared, integrated 2D observation images with various noise levels, and (c) the reconstruction results from the TV-BM3D, AL and TwIST algorithms for cases of various noise levels; averaged (d) PSNR (dB) and (e) SSIM results of images reconstructed by the TV-BM3D (red circles), AL (black squares) and TwIST (blue triangles) algorithms.

some undesirable noise points to the images during reconstruction. To further show their differences, we calculate the peak signal to noise ratio (PSNR) and structural similarity (SSIM) values of each image recovered from the three algorithms, and corresponding results are shown in Fig. 3(b) and (c), respectively. As expected, the results from the TV-BM3D algorithm is far superior to those from both the AL and TwIST algorithms.

Another dynamic scene used for our simulations is a rotating fan with three blades with different shapes. The dynamic scene also consists of 8 images, and the size of each frame is 256 × 256, as shown in Fig. 4(a). Here, the fan is fixed at its central axis, around which the blades rotate in a random way. We intentionally add Gaussian white noise of different levels to the integrated 2D observation images to test the reconstruction robustness of the TV-BM3D, AL and TwIST algorithms. Fig. 4(b) shows the observation images of various noise levels, as indicated by the signal-to-noise ratio (SNR). The dynamic scenes are reconstructed from the observation images using the above three algorithms with the SNR=25, 20, 15 and 10 dB, respectively. Fig. 4(c) shows the odd frames of the reconstructed images. A specific region of the 7th frame is zoomly shown in the inset. In order to quantitatively assess the quality of reconstructed images, the averaged PSNR and SSIM results of all the images at different noise levels are evaluated, and the results are shown in Fig. 4(d) and (e), respectively. As one can see, the TV-BM3D algorithm outperforms both the AL and the TwIST algorithms in terms of quality parameters for image reconstruction, especially for cases of low SNR. One thing worth pointing is the less descending slopes on the SNR dependence of both PSNR and SSIM values from the TV-BM3D algorithm compared with those from the AL algorithm. This clearly indicates the robust anti-noise performance of the TV-BM3D algorithm for image reconstruction.

As shown above, we have proven from numerical simulations that the TV-BM3D algorithm brings higher image quality and possesses stronger noise immunity in the image reconstruction for CUP than the conventional AL and TwIST algorithms. Next, we further compare the performances of the three image reconstruction algorithms with experimentally captured image information of an ultrashort dynamic scene. We measure the spatiotemporal intensity evolution of a spatially mod-

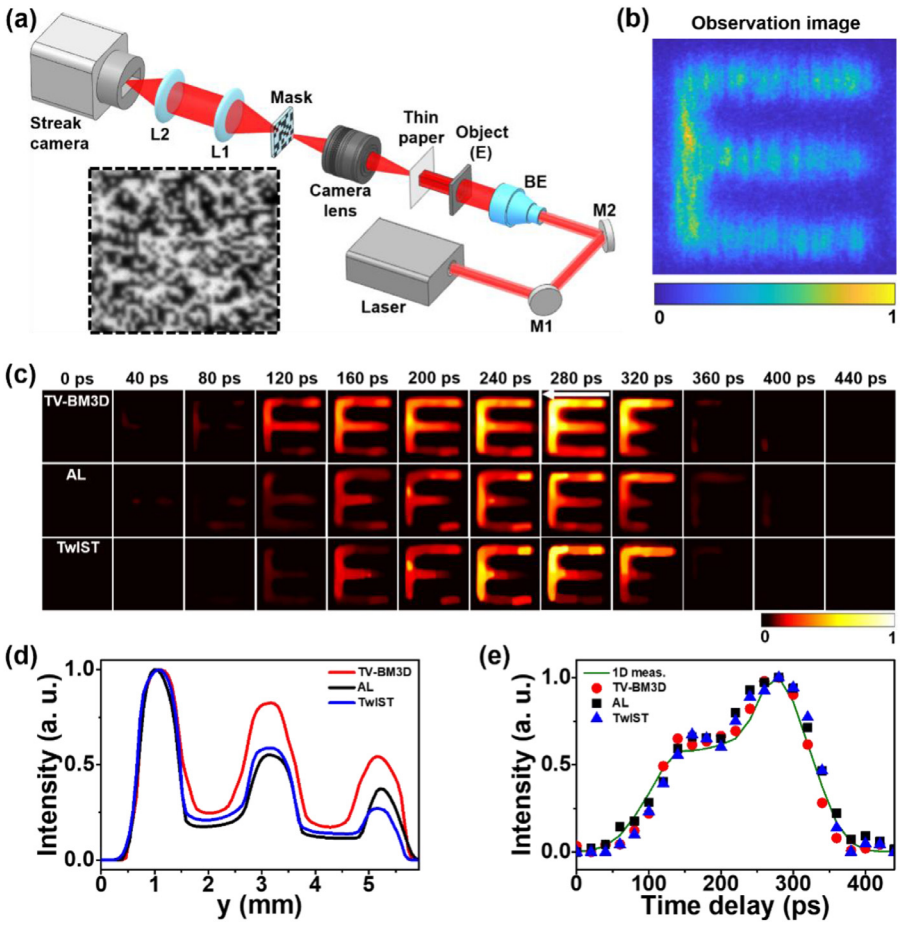

Fig. 5. (a) Experimental setup for the spatiotemporal measurement of E-shaped laser pulse, BE: beam expander, inset: a temporally unsheared CCD image of the encoding mask; (b) the sheared, integrated 2D observation image captured by internal CCD; (c) reconstructed images by TV-BM3D, AL and TwIST algorithms; (d) integrated intensities along horizontal direction for the reconstructed images of the TV-BM3D (red line), AL (black line) and TwIST (blue line) algorithms at the time delay of 280 ps; (e) extracted temporal intensity evolutions from the reconstruction results of the TV-BM3D (red circles), AL (black squares) and TwIST (blue triangles) algorithms, together with the measured result by 1D streak camera (green line).

ulated picosecond laser pulse in experiment. Fig. 5(a) shows the experimental arrangement. A single laser pulse of ~200 ps temporal width and ~800 nm central wavelength is ejected from a mode-locked Ti:Sapphire laser amplifier. The output laser pulse is spatially expanded to illuminate a hollow letter E fabricated in a black nylon plate. The photons within the shape of E can pass through the nylon plate, while those outside are blocked. The resulted E-shaped laser pulse is projected onto a thin piece of white paper, and then imaged via a camera lens onto a transmissive encoding mask with a pseudo-random binary array of pixel size 80 μm × 80 μm. Finally, the encoded dynamic scene is sent to a wide-open streak camera (Hamamatsu, C7700) for temporal shearing and spatiotemporal integration by a 4f imaging configuration. Fig. 5(b) shows the sheared, integrated 2D image finally obtained. The image of the encoding mask obtained by CUP in static mode is shown in the inset of Fig. 5(a) as well. It is worth noting that the intensity distribution of the mask obtained by the imaging system is not binary due to the presence of noise. What's worse, the random codes loaded on the dynamic scene further result in aberrations and distortions, which raise challenges for experimentally reconstructing images with high quality.

Based on the captured 2D image and encoding mask, we use the aforementioned three algorithms to reconstruct the spatiotemporal evolution of the E-shaped laser pulse, and corresponding results are shown in Fig. 5(c). Here, a total of 24 frames of images were reconstructed, but only 12 frames are represented for display. As one can see, the TV-BM3D algorithm clearly restores the E-shaped spatial structure, and the entire spatiotemporal evolution of the E-shaped laser spot from appearance to disappearance is well observed. However, the reconstructed results from the AL and TwIST algorithms fail to fully display the spatial profile of the E-shaped laser pulse even at the time delay of 280 ps with the highest light intensity. We integrate the signal intensity of the E-shaped laser profile at the time delay point of 280 ps along the horizontal direction (shown by the white arrow in Fig. 5(c)) from three algorithms, respectively. And the corresponding normalized results are given in Fig. 5(d). Compared to the AL and TwIST algorithms, the TV-BM3D algorithm offers a much higher signal-to-noise ratio for the reconstructed images, particularly for the areas corresponding to the middle and bottom horizontal strokes of the E character, as can be seen from Fig. 5(d). Information of the temporal evolution of the laser pulse intensity is also extracted for further comparison and shown in Fig. 5(e). The green line for reference indicates the time evolution of the pulse intensity measured by the one-dimensional (1D) streak camera with its entrance slit being narrowed to a few micrometers for spatial sampling [26]. Fig. 5(e) shows that all the data extracted from reconstructed images are highly consistent with the reference line, manifesting these algorithms' capabilities for image reconstruction in CUP. However, the experimental results presented here indicate that the TV-BM3D algorithm is capable of reconstructing better images of dynamic scenes in CUP operation than both the AL and TwIST algorithms.

4. Conclusions

In summary, we have developed a TV-BM3D algorithm for CUP to reconstruct the images of ultrafast dynamic scenes. Two numerical simulations and one experiment were conducted to check the reconstruction capacity of the TV-BM3D algorithm. Compared with the widely used AL and TwIST algorithms in CUP, the algorithm newly proposed here can provide higher image reconstruction quality and possess stronger noise immunity. Moreover, the framework of the TV-BM3D algorithm is plug-and-play, and any effective denoiser can be incorporated into this framework, which means that various kinds of image prior information can

be exploited during reconstruction. Therefore, the framework is flexible and versatile. Notably, many deep learning-based strategies have been developed in recent years [27-29], which can either be plugged into the existed algorithms or directly used for the image reconstruction in CUP. Compared with traditional algorithms, deep learning-based image reconstruction methods driven by a large amount of data can learn richer image priors and the inherent characteristics of the image structure. It is prospected that these improvements are very beneficial for extending the applications of CUP in capturing complex physical and biological dynamics.

Declaration of Competing Interest

We declare that we have no conflict of interest.

Acknowledgments

This work was partially supported by the National Natural Science Foundation of China (Grant Nos. 91850202, 11774094, 12074121, 11804097, 11727810 and 12034008), the Science and Technology Commission of Shanghai Municipality (Grant Nos. 19560710300 and 20ZR1417100).

Supplementary materials

Supplementary material associated with this article can be found, in the online version, at doi:10.1016/j.optlaseng.2020.106475.

References

[1] Liang J, Wang L. Single-shot ultrafast optical imaging. Optica 2018;5:1113–27.
[2] Tiwari V, Sutton M, McNeill S. Assessment of high speed imaging systems for 2D and 3D deformation measurements: methodology development and validation. Exp Mech 2007;47:561–79.
[3] Kodama R, Okada K, Kato Y. Development of a two-dimensional space-resolved high speed sampling camera. Rev Sci Instrum 1999;70:625–8.
[4] Dresselhaus-Cooper L, Gorfain J, Key C, Ofori-Okai B, Ali S, Martynowych D, et al. Single-Shot Multi-Frame Imaging of Cylindrical Shock Waves in a Multi-Layered Assembly. Sci Rep 2019;9:3689.
[5] Scott R, Perez F, Santos J, Ridgers C, Davies J, Lancaster K, et al. A study of fast electron energy transport in relativistically intense laser-plasma interactions with large density scalelengths. Phys Plasmas 2012;19:053104.
[6] Fuchs J, Nakatsutsumi M, Marques J, Antici P, Bourgeois N, Grech M, et al. Space and time-resolved observation of single filaments propagation in an underdense plasma and of beam coupling between neighbouring filaments. Plasma Phys Controlled Fusion 2007;49:B497–504.
[7] Gao L, Liang J, Li C, Wang L. Single-shot compressed ultrafast photography at one hundred billion frames per second. Nature 2014;516:74–7.
[8] Liang J, Zhu L, Wang L. Single-shot real-time femtosecond imaging of temporal focusing. Light Sci Appl 2018;7:466–75.
[9] Qi D, Zhang S, Yang C, He Y, Cao F, Yao J, et al. Single-shot compressed ultrafast photography: a review. Adv Photonics 2020;2:014003.
[10] Mochizuki F, Kagawa K, Okihara S, Seo M, Zhang B, Takasawa T, et al. Single-event transient imaging with an ultra-high-speed temporally compressive multi-aperture CMOS image sensor. Opt Express 2016;24:4155–76.
[11] Liang J, Ma C, Zhu L, Chen Y, Gao L, Wang L. Single-shot real-time video recording of a photonic Mach cone induced by a scattered light pulse. Sci Adv 2017;3:e1601814.
[12] Cao F, Yang C, Qi D, Yao J, He Y, Wang X, et al. Single-shot spatiotemporal intensity measurement of picosecond laser pulses with compressed ultrafast photography. Opt Lasers Eng 2019;116:89–93.
[13] Yang C, Cao F, Qi D, He Y, Ding P, Yao J, et al. Hyperspectrally Compressed Ultrafast Photography. Phys Rev Lett 2020;124:023902.
[14] Kim T, Liang J, Zhu L, Wang L. Picosecond-resolution phase-sensitive imaging of transparent objects in a single shot. Sci Adv 2020;6 eaay6200.
[15] Zhu L, Chen Y, Liang J, Xu Q, Gao L, Ma C, et al. Space- and intensity-constrained reconstruction for compressed ultrafast photography. Optica 2016;3:694–7.
[16] Yang C, Qi D, Wang X, Cao F, He Y, Wen W, et al. Optimizing codes for compressed ultrafast photography by genetic algorithm. Optica 2018;5:147–51.
[17] Yang C, Qi D, Cao F, He Y, Wang X, Wen W, et al. Improving the image reconstruction quality of compressed ultrafast photography via an augmented Lagrangian algorithm. J Opt 2019;21:035703.
[18] Liao X, Li H, Carin L. Generalized alternating projection for weighted-$l_{2,1}$ minimization with applications to model-based compressive sensing. SIAM J Imag Sci 2014;7:797–823.
[19] Bioucas-Dias J, Figueiredo M. A new TwIST: two step iterative shrinkage/thresholding algorithms for image restoration. IEEE Trans Image Process 2007;16:2992–3004.
[20] Berg E, Friedlander M. Probing the Pareto frontier for basis pursuit solutions. SIAM J Sci Comput 2008;31:890–912.
[21] Tofighi M, Kose K, Cetin A. Denoising using projections onto the epigraph set of convex cost functions. IEEE Int Conf Image Process 2015:2709–13.
[22] Shi B, Lian Q, Huang X, An N. Constrained phase retrieval: when alternating projection meets regularization. J Opt Soc Amer B 2018;35:1271–81.
[23] Yuan X. Generalized alternating projection based total variation minimization for compressive sensing. IEEE Int Conf Image Process 2016:2539–43.
[24] Dabov K, Foi A, Katkovnik V, Egiazarian K. Image denoising by sparse 3d transform-domain collaborative filtering. IEEE Trans Image Process 2007;16:2080–95.
[25] Yuan X, Yang L, Suo J, Dai Q. Plug-and-Play Algorithms for Large-scale Snapshot Compressive Imaging. ArXiv 2020;2003:13654.
[26] Guide to streak cameras, https://www.hamamatsu.com/resources/pdf/sys/SHSS0006E_STREAK.pdf [accessed 12-August-2020].
[27] Zhang K, Zuo W, Zhang L. FFDNet: toward a fast and flexible solution for CNN based image denoising. IEEE Trans Image Process 2017;27:4608–22.
[28] Zhang K, Zuo W, Gu S, Zhang L. Learning deep CNN denoiser prior for image restoration. CVPR 2017:2808–17.
[29] Ma Y, Feng X, Gao L. Deep-learning-based image reconstruction for compressed ultrafast photography. Opt Lett 2020;45:4400–3.